

JGR Space Physics

RESEARCH ARTICLE

10.1029/2021JA029143

This article is a companion to Birn et al. (2021), <https://doi.org/10.1029/2021JA029184>.

Key Points:

- A propagating dipolarization front can accelerate O^+ ions to form a field-aligned plasma sheet boundary layer (PSBL) beam just as with protons
- Beam particles originate from the opposite lobes or PSBL at a higher adiabaticity, but from the central plasma sheet at a low adiabaticity
- Close to the boundary, O^+ beams are less pronounced than H^+ beams due to a slower speed and an equatorward drift after acceleration

Correspondence to:

J. Birn,
jbirn@spacescience.org

Citation:





Birn, J., Hesse, M., Bingham, S. T., Turner, D. L., & Nakamura, R. (2021). Acceleration of Oxygen Ions in Dipolarization Events: 2. PSBL distributions. *Journal of Geophysical Research: Space Physics*, 126, e2021JA029143. <https://doi.org/10.1029/2021JA029143>

Received 16 JAN 2021

Accepted 4 MAY 2021

© 2021. American Geophysical Union.
All Rights Reserved.

Acceleration of Oxygen Ions In Dipolarization Events: 2. PSBL Distributions

J. Birn^{1,2} , M. Hesse^{3,4} , S. T. Bingham⁵, D. L. Turner⁵ , and R. Nakamura⁶ 

¹Space Science Institute, Boulder, CO, USA, ²Los Alamos National Laboratory, Los Alamos, NM, USA, ³Department of Physics and Technology, University of Bergen, Bergen, Norway, ⁴NASA Ames Research Center, Moffett Field, CA, USA, ⁵Space Exploration Sector, The Johns Hopkins University Applied Physics Laboratory, Laurel, MD, USA, ⁶Space Research Institute, Austrian Academy of Sciences, Graz, Austria

Abstract This paper represents the second part of an investigation of the acceleration of energetic oxygen ions from encounters with a dipolarization front (DF), based on test particle tracing in the fields of an MHD simulation. In this paper, we focus on distributions in the plasma sheet boundary layer (PSBL). O^+ beams close to the plasma sheet boundary are found to be less pronounced and/or delayed against the H^+ beams. The reason is that these particles are accelerated by nonadiabatic motion in the duskward electric field such that O^+ ions gain the same amount of energy, but only 1/4 of the speed of protons. This causes a delay and larger equatorward displacement by the $\mathbf{E} \times \mathbf{B}$ drift. In contrast, the O^+ beams somewhat deeper inside the plasma sheet, where previously multiple proton beams were found, are accelerated at an earthward propagating DF just like H^+ , forming a field-aligned beam at a similar speed as the lowest-energy H^+ beam. We found that the source location depends on the adiabaticity of the orbit. For larger adiabaticity, the beam ions originate initially from the outer plasma sheet, but later from the opposite PSBL or lobe, but for low adiabaticity, sources are well inside the plasma sheet. The energy gained from a single encounter of a DF is comparable to the kinetic energy associated with the front speed. Assuming maximum speeds of 500–1,000 km/s, this yields a mass dependent acceleration of about 1–5 keV for protons and 20–80 keV for oxygen ions, independent of their charge state.

1. Introduction

The presence of oxygen ions in the geomagnetic tail and their important role in contributing to the total pressure, and as a source population to ring current enhancement has been demonstrated by a large number of investigations (e.g., Keika et al., 2013, 2018; Kistler et al., 2016; Kronberg et al., 2017; Liao et al., 2014, 2015; H. Zhao et al., 2015). There is strong evidence that oxygen ions are energized by the dynamic reconfigurations of the near tail, particularly in substorms (e.g., Bingham et al., 2021; Keika et al., 2013; Kronberg et al., 2015; Nosé, Lui, et al., 2000; Nosé, Ohtani, et al., 2000). This study represents the second part of an investigation on the acceleration of oxygen ions by earthward propagating dipolarization fronts (DFs) (Nakamura et al., 2002; Runov et al., 2009) or rapid flux transport events (RFTs) (Schödel et al., 2001), focusing particularly on effects near the plasma sheet boundary, while the first part (Birn, Bingham, Turner, and Hesse, Acceleration of Oxygen Ions in Dipolarization Events: 1. CPS Distributions, submitted to the Journal of Geophysical Research, hereafter called “paper 1”), focused on the central plasma sheet (CPS).

The present investigation was motivated in part by the Magnetospheric Multiscale (MMS) observations of multiple field-aligned beams, observed simultaneously at different energy near the plasma sheet boundary on June 23, 2015 (Birn et al., 2017). These beams were interpreted as a combination of proton beams accelerated at a near-tail reconnection site, or by single or multiple encounters of an earthward propagating DF with intermediate mirroring closer to Earth. However, before and after that event the presence of oxygen was documented, both in the plasma sheet boundary layer (PSBL) and the adjacent lobe (Reiff et al., 2016). This suggested the possibility that at least a part of the multiple beams could be attributed to accelerated O^+ ions as well. Energy dispersed O^+ flux enhancements, apparently originating from the lobe, were also found recently by S. J. Zhao et al. (2019), on the basis of Cluster observations in relation to dipolarization events. However, it is not obvious that the mechanism that causes the acceleration of the proton beam would accelerate oxygen ions to the same speed (which would show up as an apparent beam of quadruple speed if mistaken for hydrogen). Therefore, one part of the present investigation addresses O^+ distribution functions

Table 1
Characteristic Parameter Sets Chosen for the Particle Tracing

Parameter	Set A	Set B
$L_n(R_E)$	1.5	1.5
B_n (nT)	12.56	25.11
v_n (km/s)	1,000	500
t_n (s)	9.6	19.1
E_n (mV/m)	12.56	12.56
W_n (keV)	5.22	1.30
$\sigma(O^+)$	0.72	2.9
$\sigma(H^+)$	11.5	46

at the same location where the multiple proton beams have been identified in the previous simulation (Birn et al., 2017). In addition, we chose a location farther tailward, but closer to the plasma sheet boundary, where single field-aligned H^+ beams had been identified and analyzed in an earlier paper (Birn et al., 2015).

2. Simulation Approach

The basic approach has been described in more detail in paper 1. It is based on an MHD simulation (Birn et al., 2011), involving a reconnection in the near magnetotail, associated with a collapse (dipolarization) of the inner tail region, fast flows, and earthward propagating dipolarization fronts (Birn et al., 2011). Dimensionless quantities are used in the simulation, normalized by a length scale L_n (plasma sheet half-width), magnetic field B_n (lobe field), and velocity v_n (Alfvén speed based on B_n and a plasma sheet density; all units taken near the later reconnection site). This yields a time unit $t_n = L_n/v_n$ and electric field $E_n = v_n B_n$; characteristic values chosen are shown in Table 1.

The simulation covers a region $0 \geq x \geq -60$, with a dipole outside the box at $x = 5$. The evolution includes a phase of slow externally driven influx at the high latitude boundaries, leading to the formation of a thin embedded current sheet in the near tail. The dynamic evolution is initiated (at $t = 61$) by imposing a finite resistivity in the region of the thin current sheet. Slow magnetic reconnection starts at $t \approx 90$ near $x = -9$, but becomes faster with a rapid flow burst centered at midnight after $t > 120$. The maximum rate of energy dissipation associated with this flow burst occurs around $t \approx 130$. The simulation also includes subsequent flow bursts off midnight, which have not been considered here.

Figure 1 shows a snapshot of the color-coded cross-tail electric field E_y (panel c) indicating the RFT event, together with magnetic flux contours (The sequence of propagation of the RFT is illustrated in Figure 2 of paper 1). The plus signs indicate two locations where ion particle fluxes are evaluated; the MHD simulation magnetic and electric field components at these locations are shown in panels a and b as functions of time. It is noteworthy that the electric field, normalized in the common way by $v_n B_n$, reaches a value of about 0.2 at the reconnection site, but significantly higher values close to unity in the collapsing field of the dipolarization front, as demonstrated in Figure 1c.

Using suitable interpolation of the magnetic and electric fields from the MHD simulation, we integrated the full ion orbits backward in time from the selected times and the chosen locations until they reached the boundary of the simulation box or the initial state ($t = 61$). At the near-Earth boundary, the particles were reflected back into the box, taking into account a delay from mirroring closer to Earth, but neglecting the

Using suitable interpolation of the magnetic and electric fields from the MHD simulation, we integrated the full ion orbits backward in time from the selected times and the chosen locations until they reached the boundary of the simulation box or the initial state ($t = 61$). At the near-Earth boundary, the particles were reflected back into the box, taking into account a delay from mirroring closer to Earth, but neglecting the

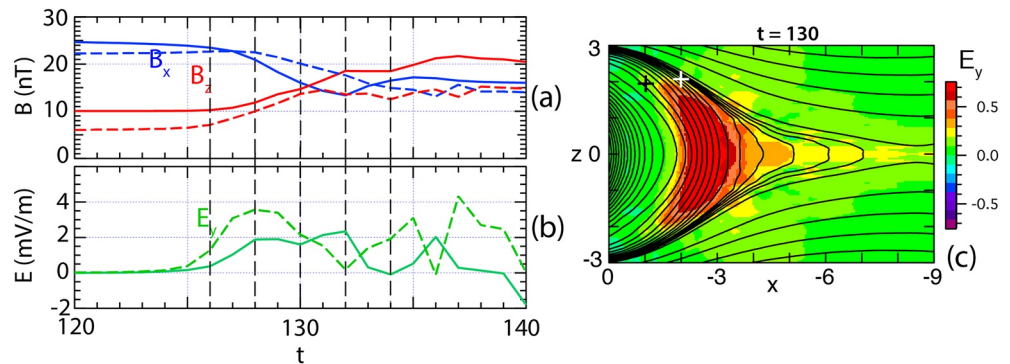


Figure 1. Temporal variations of (a) the magnetic field and (b) the electric field in the MHD simulation at two locations, $(-1,0,1.9)$ (solid lines) and $(-2,0,2.1)$ (dashed lines). These location are indicated by the plus signs in the panel (c), superposed on the color-coded electric field E_y in the x, z plane at $t = 130$ (corresponding to the central panel of Figure 2 in paper 1). The vertical dashed lines in panels (a) and (b) indicate times at which velocity distributions had been evaluated. Magnetic field units are based on the parameter set A in Table 1.

loss cone and disregarding the potential injection of ionospheric particles. Fluxes of particles at the chosen locations and different times have been evaluated by applying Liouville's theorem of the conservation of phase space density, f , along phase space trajectories and imposing initial distributions, chosen as kappa distributions (Equation 4 of paper 1).

As also discussed in paper 1, we chose isotropic initial distributions with the same initial temperatures for oxygen and hydrogen, and an oxygen density proportional to the hydrogen density. While this appears reasonable when the source location is inside the plasma sheet (e.g., Frank et al., 1977; Peterson et al., 1981), the assumption of isotropy becomes questionable, particularly when the source is in the lobes or the plasma sheet boundary layer where the source population is expected to result from ionospheric outflow. This is discussed in more detail further below.

Table 1 also contains two additional quantities. One is a characteristic energy unit, defined by $W_n = \frac{1}{2} m_p v_n^2$, where m_p is the proton mass, (such that proton energy is given by $W_n v^2$ and oxygen energy by $16W_n v^2$, where v is the dimensionless speed). The other is the dimensionless parameter σ given by

$$\sigma = \omega_{ci} t_n = \frac{q B_n}{m_i} t_n \quad (1)$$

where ω_{ci} is the ion gyro frequency based on the magnetic field B_n and the charge q . For protons, the parameter σ is equal to L_n/d_i , where d_i is the ion inertial length, while for singly charged oxygen ions it is

$$\sigma = \sqrt{\frac{m_p}{m_o}} \frac{L_n}{d_i} \quad (2)$$

The definition of σ in Equation 1 makes it clear that for large values ($\sigma \gg 1$), that is, for many gyration periods within a characteristic time scale for the MHD evolution, the particle orbits are more adiabatic. However, σ describes a general current sheet characteristic; the instantaneous particle behavior differs depending on its energy.

Oxygen orbits have been integrated for two values of σ , corresponding to the two unit sets defined in Table 1, $\sigma = 0.72$ and $\sigma = 2.9$. It is noteworthy that even when a specific length scale (here, $L_n = 1.5R_E$) and a parameter σ are chosen, the results can still be scaled to different units by multiplying the magnetic field and velocity by a factor λ , the time by a factor $1/\lambda$, and the electric field and particle energy by a factor λ^2 . For that reason, we mostly keep the dimensionless units for the following results.

3. PSBL Distributions at (−1, 0, 1.9)

In this section we evaluate the O^+ distribution functions at the PSBL location $x = -1, y = 0, z = 1.9$ (shown by the black plus sign in Figure 1c), where previously (Birn et al., 2017) the multiple proton beams have been found. Distribution functions were evaluated at three times, $t = 128, 130,$ and 132 , near the beginning, middle, and end of this dipolarization, indicated by the three middle vertical dashed lines in panels a and b of Figure 1.

The distribution functions at the chosen location are shown in Figure 2 as functions of v_x and v_z , panels a–c for protons with $\sigma = 11.5$ (based on parameter set A in Table 1), and (right columns) O^+ ions, (d–f) for $\sigma = 0.72$ and (g–i) for $\sigma = 2.9$, respectively. The proton distributions correspond to those in Birn et al. (2017, Figures 4d–4f). The proton distributions for parameter set B with $\omega_{ci} t_n = 46$ are very similar to those for set A and are not shown here.

The oxygen distributions develop field-aligned beams at about the same speed as the lowest hydrogen beam with $v_{\text{beam}} \approx 1$, corresponding to 1,000 km/s for parameter set A (Figures 2a–2f) and 500 km/s for set B (Figures 2g–2i). No pronounced return beams or higher energy beams are visible in the oxygen distributions. This is primarily due to the fact that the return beams and the higher energy beams require higher initial speeds. Since we chose the same source temperature for oxygen as for hydrogen and the same kappa distri-

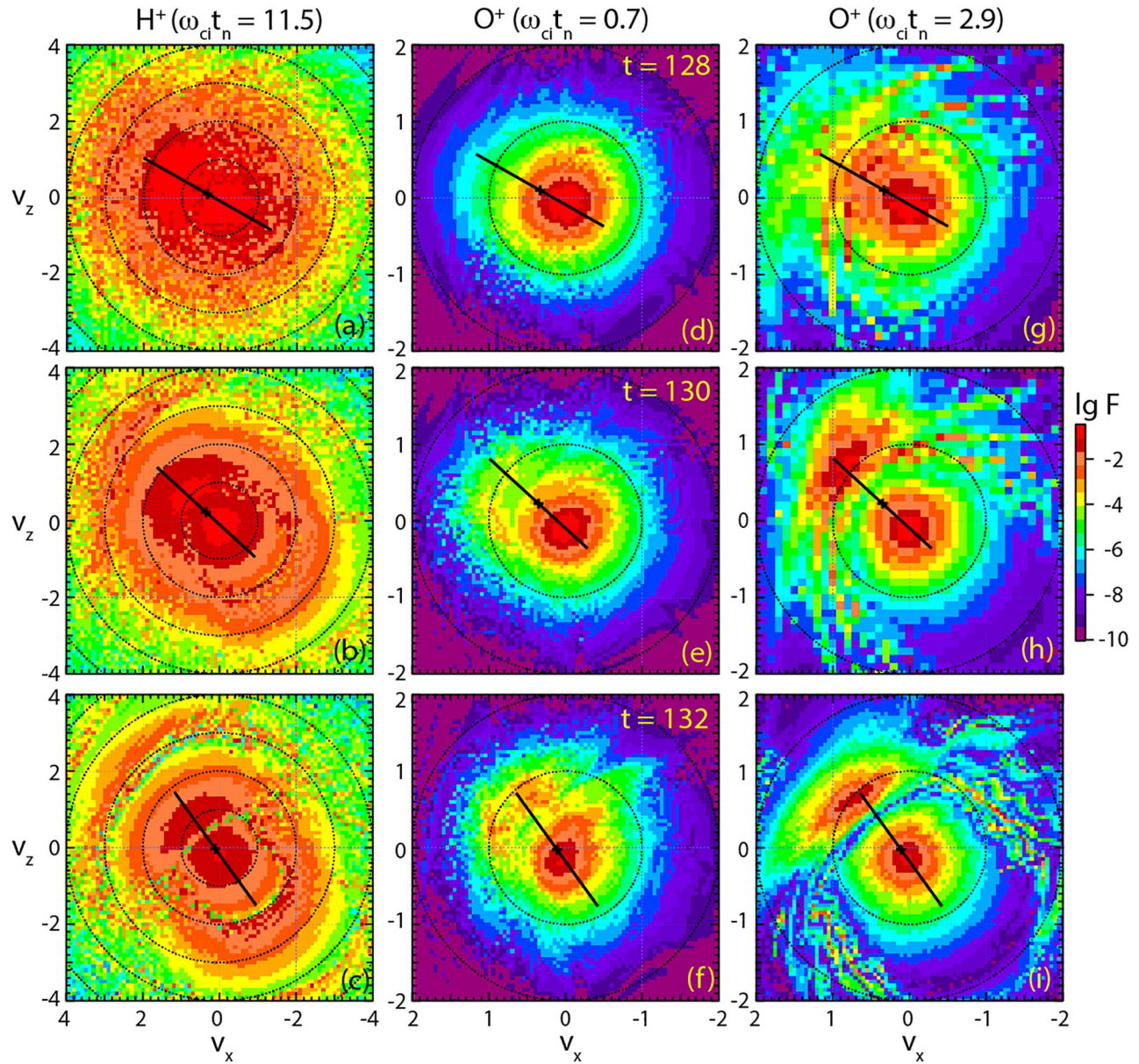


Figure 2. Ion velocity distributions at the location $x = -1, y = 0, z = 1.9$ for three times, $t = 128, 130, 132$, indicated in Figure 1, (a–c) for protons and (d–f) for O^+ ions, based on parameter set A, and (g–i) for O^+ ions, based on parameter set B. Note that the velocity unit for (a–f) is 1,000 km/s, while it is 500 km/s for (g–i). The plus signs indicate the MHD flow velocity and the black bar, the magnetic field direction and magnitude.

bution, the thermal speed is lower for oxygen by a factor of 1/4 and the source distributions fall off much more rapidly as functions of velocity.

As discussed in Section 2, the oxygen distributions were constructed assuming isotropic source distributions with a density proportional to the hydrogen density. To check whether this assumption is appropriate, we investigated the source locations and initial velocities of the particles contributing to the core and beam populations in Figures 2f and 2i. Figures 3a–3c show core (blue pixels) and beam populations (red pixels) at $t = 132$ for $\sigma = 0.72$, and $t = 130$ as well as $t = 132$ for $\sigma = 2.9$, selected using the largest f values. Figures 3d–3f show the locations in x and z of the origins together with magnetic flux contours, while panels g–i show the initial velocity distributions. The initial locations demonstrate a characteristic difference between parameter sets A ($\omega_{ci}t_n = 0.72$) and B ($\omega_{ci}t_n = 2.9$).

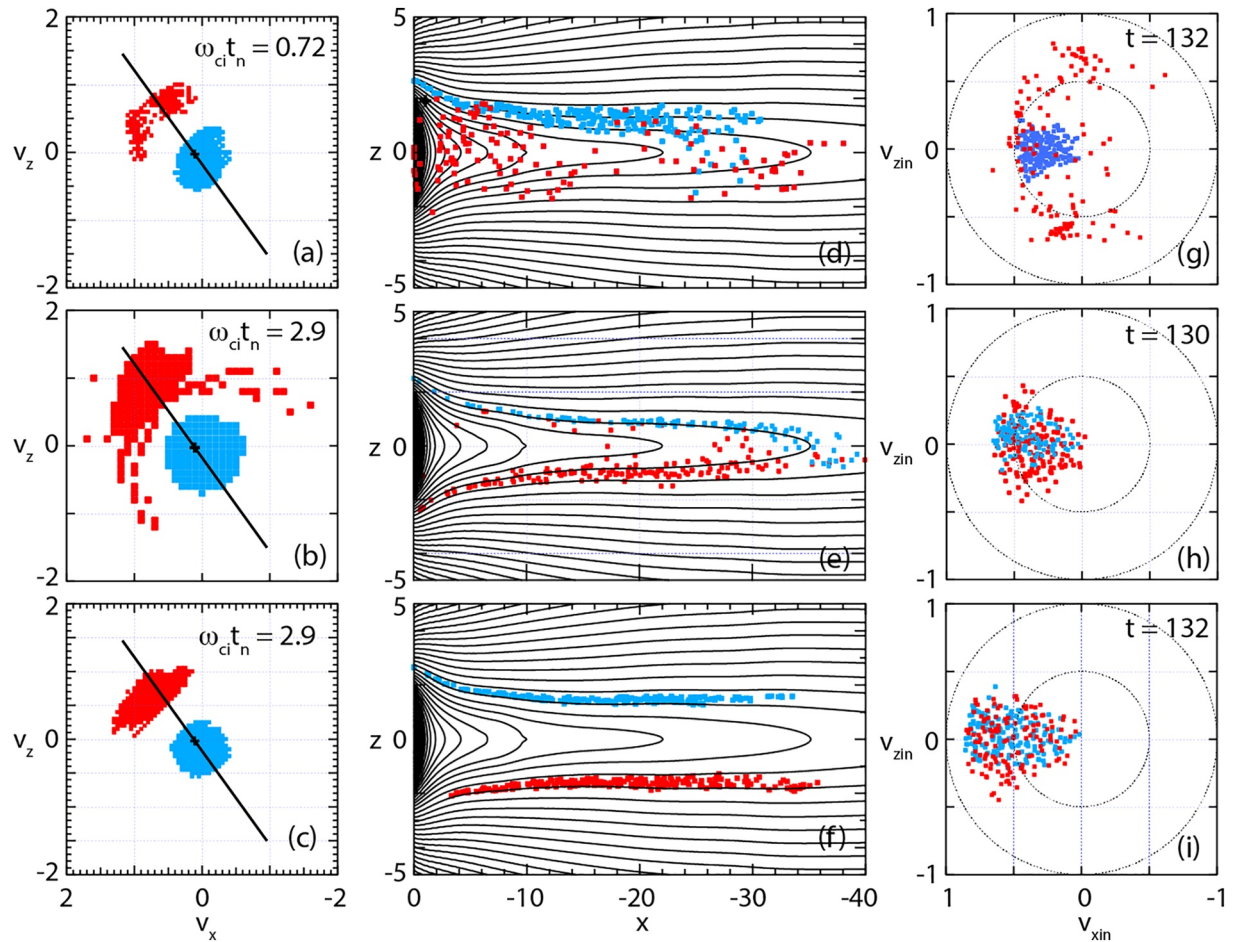


Figure 3. Origins of the O^+ ions contributing to the core and beam populations in Figure 2. The left panels (a–c) show the velocities of the beam (red pixels) and core populations (blue pixels), choosing the top f values from Figures 2f, 2h, and 2i, respectively; the plus sign and the black line, again, show the MHD flow velocity and the magnetic field direction, respectively. The center panels (d–f) show the source locations of these core and beam populations in x and z , superposed on the magnetic field at the initial time $t = 61$, and the right panels (g–i) show the initial velocities. The top row (a, d, and g) corresponds to $\omega_{ci}t_n = 0.72$ and $t = 132$, the middle row (b, e, and h) to $\omega_{ci}t_n = 2.9$ and $t = 130$, and the bottom row (c, f, and i) to $\omega_{ci}t_n = 2.9$ and $t = 132$.

For $\omega_{ci}t_n = 2.9$ (parameter set B), both the core and the beam populations observed at $t = 130$ originate from field lines extending into the distant plasma sheet (Figure 3e), denoted as "outer CPS" in paper 1, but later, at $t = 132$, from regions adjacent to the plasma sheet (Figure 3f), that would be identified as "plasma sheet boundary layer," according to the definition given in paper 1. However, the choice of the boundary between the PSBL and lobes is somewhat arbitrary, such that they might also be attributable to the adjacent lobes. They both have similar low energy source populations (Figures 3h and 3i) with earthward directed velocities. Both increase on average for the distributions observed at the later time, $t = 132$. While our initial distributions account for a significant decrease in density from the plasma sheet toward the lobes, they do not account for the fact that the likely source of O^+ populations is the outflow from the ionosphere, such that the source populations would be expected to stream tailward in the PSBL or adjacent lobes. This makes it less likely that ionospheric outflow could contribute significantly to these source populations at the later time. The situation might be similar if these ions were of solar wind origin entering through the high-latitude lobe with a tailward velocity component.

However, the results on the source locations and velocities have to be taken into account with some caution. Our near-Earth boundary condition causes all particles that cross the inner boundary to be reflected back into the tail. Some of those might actually have been of ionospheric origin instead. Furthermore, the particles that contribute to the peak of the beam distribution have the lowest source energy. Insufficient

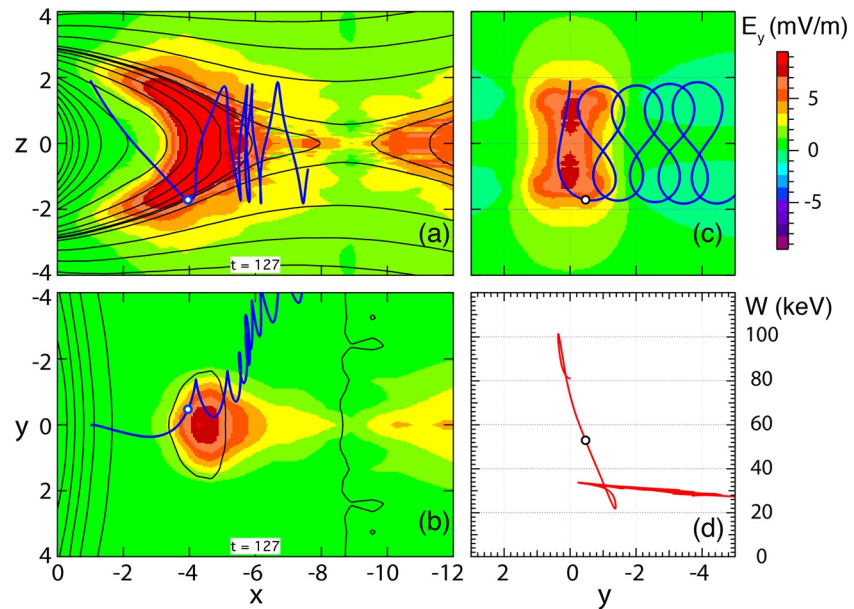


Figure 4. Characteristic orbit of an O^+ ion contributing to the beam in Figure 2f with $\omega_{ci}t_n = 0.72$, overlaid on snapshots of the cross-tail electric field E_y at $t = 127$ (color): (a) projected into the $y = 0$ plane, (b) into the $z = 0$ plane, and (c) into the $x = -4$ plane; (d) particle energy as function of y . The black lines in panels (a and b) are the magnetic flux contours and contours of constant B_z , respectively, the same as in Figure 2 of paper 1. The arrowhead indicates the endpoint of the orbit and the white dot shows the location of the particle at $t = 127$ near the major energy increase.

resolution of this phase space region might not show particles with very low, but tailward initial speed. Both of these effects need further exploration.

In contrast to the case $\omega_{ci}t_n = 2.9$, the beam population for $\omega_{ci}t_n = 0.72$ (case A) originates in the central plasma sheet, while the core population comes mostly from the PSBL (Figure 3d). The latter may require a similar ionospheric outflow as the lobe populations and thus, may also not be observable. However, the beam population may be observable when the plasma sheet contains a significant oxygen ion population. In contrast to case B, the source population of the beam now has a somewhat higher temperature than the source of the core, albeit with a velocity still mostly below $v = 0.5$ (corresponding to 20.9 keV).

Figures 4a–4c illustrate a typical orbit of an O^+ ion contributing to the beam in Figure 2f for $\omega_{ci}t_n = 0.72$, shown in three different projections. The orbit is superposed on snapshots of the electric field at $t = 127$, just prior to the time of maximum acceleration. Figure 4d shows the particle energy as a function of y . The particle initially meanders in a figure eight orbit around the neutral sheet toward midnight. When it encounters the propagating DFB south of the neutral sheet, it accelerates by moving in the direction of the cross-tail electric field. It is then turned earthward by the stronger B_z and moves northward along the magnetic field, together with the DF. Its velocity becomes more field-aligned, largely from its inertia.

The history of particles contributing to the beam in case B with $\omega_{ci}t_n = 2.9$ is quite different, as illustrated by a sample orbit in Figure 5. The particle starts out at a low energy quasi-adiabatically on a field line that, according to Figure 3e and the criterion given in paper 1, would be identified as the plasma sheet boundary layer. It moves slowly earthward while the field line is $\mathbf{E} \times \mathbf{B}$ drifting equatorward. When the field line is reconnected and the particle is caught within the dipolarizing flux bundle, it accelerates consistently with the increasing $\mathbf{E} \times \mathbf{B}$ drift speed. This (perpendicular) energy, however, becomes gradually, and eventually almost completely, converted into parallel energy, while the total energy does not increase anymore. This is similar to the acceleration of protons illustrated in Figure 7 of Birn et al. (2017). The acceleration mechanism may be identified, at least qualitatively, with the “current sheet acceleration” (Lyons & Speiser, 2014) or the “convection surge” mechanism (Quinn & Southwood, 1982). This is very similar to the history of particles contributing to the lowest-energy proton beam (Figure 6 of Birn et al., 2017) and to the particles contributing to the counter-streaming beams near the equatorial plane discussed in paper 1.

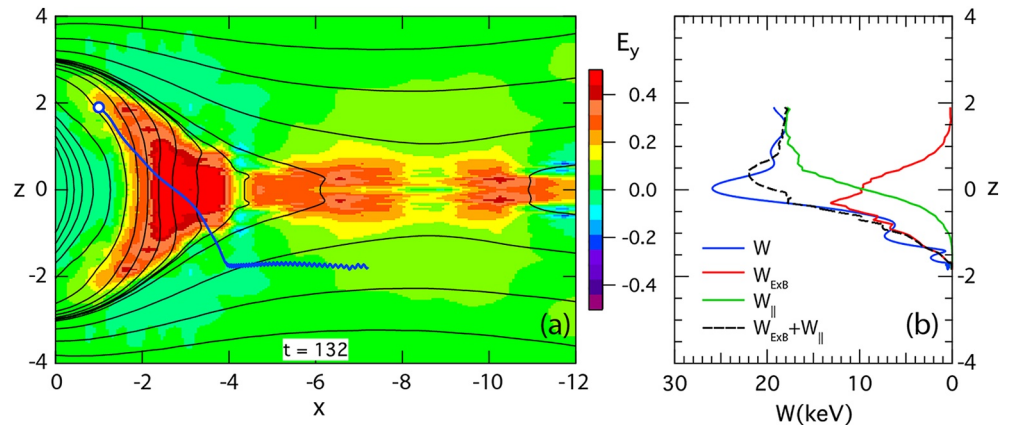


Figure 5. (a) Characteristic orbit of an O^+ ion contributing to the beam in Figure 2i with $\omega_{ci}t_n = 2.9$, overlaid on snapshots of the cross-tail electric field E_y at $t = 132$ (color), projected into the $y = 0$ plane, (b) particle energy contributions (horizontal axis) versus z . The white dot indicates the final location of the particle at $t = 132$.

4. PSBL Distributions at $(-2, 0, 2.1)$

In order to investigate how typical the PSBL results are, we have chosen another location, $(x, y, z) = (-2, 0, 2.1)$, which is closer to the boundary (but slightly farther tailward), shown by the white plus sign in Figure 1; this location has also been investigated earlier for H^+ ions (Birn et al., 2015). Figure 6 shows velocity distributions as functions of v_x and v_z at this location. The left column (panels a–e) shows the distributions for H^+ with panels a and b corresponding to the distributions in Figure 6 of Birn et al. (2015) (Note that earthward flow is now to the left.) These distributions do not show the return flow as in Birn et al. (2015). The reason is that, in the earlier investigation, particles had been reflected immediately at the inner (left) boundary without taking the delay from earthward travel and mirroring outside the box into account. The second (panels f–j) and third columns (panels k–o) show the O^+ distributions for parameter set A ($\sigma = 0.72$) and B ($\sigma = 2.9$), respectively.

It is obvious from Figure 6 that oxygen beams close to the plasma sheet boundary are not as pronounced as proton beams. For $\sigma = \omega_{ci}t_n = 0.72$, the beam starts at a later time ($t = 134$, panel j), and it is not symmetric around the magnetic field direction, indicating agyrotropy. For $\sigma = 2.9$, it is barely visible, with f values that are about nine decades lower than the maximum, showing only spotty larger enhancements at $t = 134$ (red and yellow pixels in panel o). The reason becomes clear from an inspection of orbits contributing to the beams. Figure 7 shows the projections of two orbits contributing to the beams in Figure 6, together with their energy as a function of x .

Figures 7a–7c represents an orbit for $\sigma = 0.72$, ending at the velocity indicated by a circle in Figure 6j. This particle originates from the more distant tail on a nearly adiabatic orbit and gets trapped in the inner tail due to reconnection. The projection in Figure 7a looks very similar to that of Figure 5a. However, the energy contributions in Figure 7c demonstrate that the energy gain simply stems from a non-adiabatic motion in the direction of the electric field near $x = -4.5$, and is not related to a capture by $\mathbf{E} \times \mathbf{B}$ drift. In fact, inward of $x = -4$, the particle moves earthward non-adiabatically at a speed slower than the $\mathbf{E} \times \mathbf{B}$ drift speed and its energy remains nearly unchanged.

In contrast, the particle for $\sigma = 2.9$, contributing to the barely visible, higher energy beam at $t = 128$, indicated by the circle in Figure 6l, has a different history, illustrated by Figures 7d–7f. The white circle in panel d shows its end location, while the color-coded electric field and the white circle in panel e correspond to a time near the maximum acceleration. As indicated by panel f, its initial energy is much higher, approximately 50 keV, consistent with its low initial and final f value. Therefore, it is highly non-adiabatic already before the acceleration. It exhibits a meandering orbit in the duskward direction. Its energy gain, then, is also due to a duskward displacement in the direction of the electric field. In this case, the local $\mathbf{E} \times \mathbf{B}$ drift speed is much lower. O^+ ions that contribute to the flux enhancements at later time, $t = 134$, (indicated by

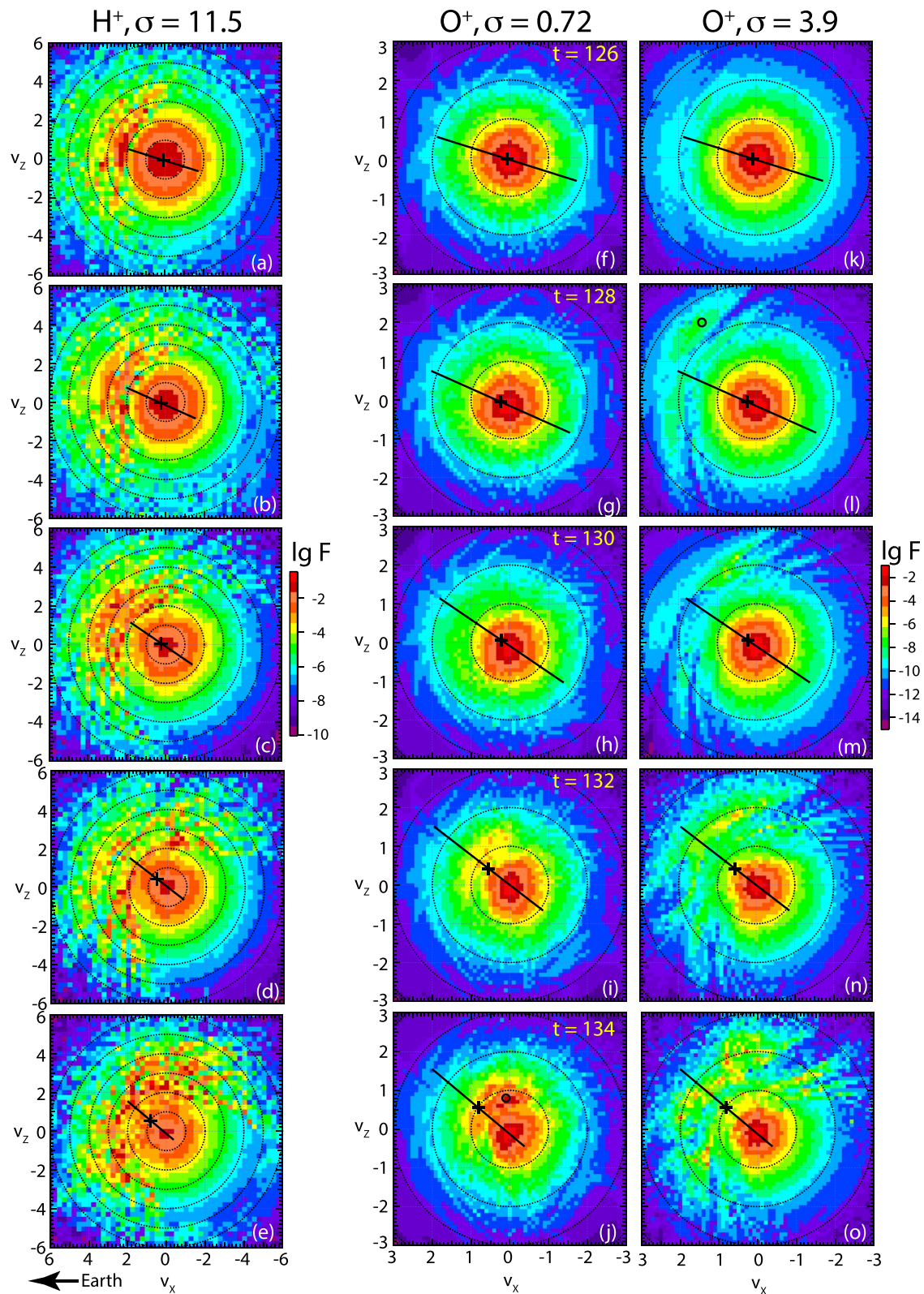


Figure 6. Ion velocity distributions at the location $x = -2, y = 0, z = 2.1$ at different times as indicated in the center column, (a–e) for protons, parameter set A, and (f–j) for O^+ ions, based on parameter set A, and (k–o) for O^+ ions, based on parameter set B. Note that the velocity unit for (a–j) is 1,000 km/s, while it is 500 km/s for (k–o). The plus signs again indicate the MHD flow velocity and the black bar indicates the magnetic field direction and magnitude. The two small black circles in panels j and l represent velocities chosen for illustrating the characteristic orbits contributing to the beams.

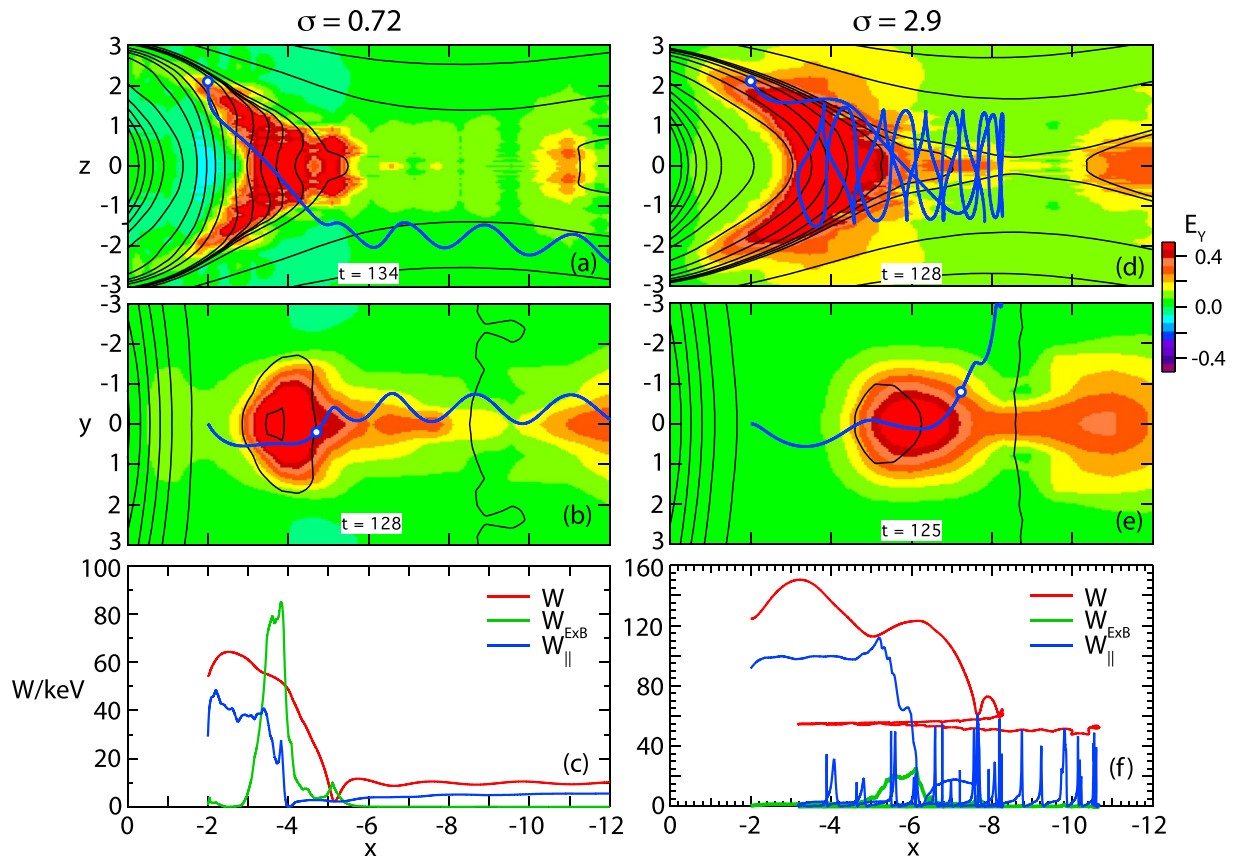


Figure 7. Characteristic orbits of O^+ ions contributing to the beams in Figures 6j and 6l, (a–c) with $\sigma = 0.72$ and (d–f) with $\sigma = 2.9$, (a, d) projected into the x, z plane at the final times, (b, e) projected into the x, y plane at a time near the maximum acceleration. The orbits are overlaid on the snapshots of the cross-tail electric field E_y (color) with the white dots indicating the locations of the particle at the selected times: (top panels) at the final time and (middle panels) at a time near the maximum acceleration. Panel (c and f) show the particle energy (red lines) with the parallel contribution (blue lines) versus x ; the green lines indicate the energy that would be associated with the local $\mathbf{E} \times \mathbf{B}$ drift at the particle location.

red and yellow pixels at $v \approx 1.5\text{--}2$ in Figure 6o) have a history similar to the one in Figures 7a–7c and are not shown here.

In either case, the energy gain stems from the non-adiabatic motion in the direction of the duskward electric field, and should, thus, be similar for O^+ as for H^+ . This means, however, that the O^+ ions have only 1/4 of the speed of the H^+ ions after ejection from the acceleration region along the magnetic field toward Earth. This fact, together with an equatorward $\mathbf{E} \times \mathbf{B}$ drift causes a displacement of oxygen ions farther inward from the plasma sheet boundary when compared to protons, which is why they become observable at the chosen location only when the plasma sheet expands sufficiently or when they are accelerated at a closer approach of the DF. Another effect might be that oxygen ions accelerated near the x -line are slower than the earthward propagating dipolarization front. Thus, O^+ ions accelerated later at the DF might be observable earlier and be dominant. This effect might be enhanced by the fact that, in our MHD simulation, the electric field, and the associated cross-tail voltage, become stronger in the propagating DF than at the x -line.

5. Summary and Conclusions

This paper represents the second part of an investigation of oxygen ion acceleration, using a three-dimensional MHD simulation of magnetotail reconnection and dipolarization of the inner tail (Birn et al., 2011) as a background for particle orbit tracing. In this paper we have focused on ion fluxes in the plasma sheet boundary layer, which may exhibit characteristic field-aligned beams (Andrews et al., 1981; Birn et al., 2015, 2017; Forbes et al., 1981; Takahashi & Hones, 1988; Zhou et al., 2012), while locations within the central plasma sheet were addressed in paper 1. As in paper 1, we used two sets of parameters, corresponding to the two

values of the adiabaticity parameter $\sigma = \omega_{ci} t_n$, where $\omega_{ci} = qB_n/m_i$ is the ion gyro frequency, B_n is a characteristic magnetic field strength, and $t_n = L_n/v_n$ is a characteristic MHD wave time scale. The values of σ chosen were below and above unity (0.72 and 2.9); orbits for large values of σ are more adiabatic. Distribution functions have been evaluated at two locations close to the plasma sheet boundary near the beginning, middle, and end of a dipolarization.

The first location, slightly earthward and equatorward from the second one has been chosen because a previous investigation showed multiple beams, both earthward and tailward in observations and simulations (Birn et al., 2017). While the simulated beams had been entirely based on accelerated protons, the observed ones might have included oxygen as well. Indeed, in the present simulation, we found that oxygen ions could be accelerated at an earthward propagating dipolarization front similarly to hydrogen ions, forming a field-aligned beam at a similar speed as the lowest-energy H^+ beam, together with a core population, which is simply transported equatorward by $\mathbf{E} \times \mathbf{B}$ drift from a higher latitude without significant heating or acceleration. The origin of the beam ions has been found to depend on the parameter σ . For the larger value of $\sigma > 1$, beam and core populations initially originated from inside the plasma sheet on field lines extending into the more distant tail, whereas at later times the origin was found in the PSBL or lobes. This is consistent with the progression of reconnection from the central plasma sheet toward the PSBL and lobes. In contrast, for the smaller value of σ , less than unity, the source location of the beam particles has been found to be inside the plasma sheet, while the core particles originated from the PSBL or adjacent lobe.

Whether the oxygen beams are actually observable critically depends also on the availability of a suitable source population, that is, on the density of the source population at the required velocities. Although oxygen ions have been observed not only inside the plasma sheet, but also in the adjacent PSBL and lobes (e.g., Orsini et al., 1984), most recently by MMS (Reiff et al., 2016), they tend to form tailward beams in the lobes consistent with their ionospheric origin. In contrast, we found that the source velocities of the earthward beams typically require an earthward component. This seems more likely for sources inside the plasma sheet. Thus, the beam might be observable when the plasma sheet contains a sufficient source of trapped oxygen ions, whereas an outflow of oxygen ions into the PSBL or lobes might not provide a suitable source. Accordingly, the oxygen beam and core might be observable only very briefly at the beginning of a dipolarization, provided again, that the plasma sheet already contains some oxygen source population.

However, this conclusion has to be considered with some caution for several reasons. First, as noted also in paper 1 concerning the counter-streaming beams in the CPS, the conclusion about the source velocities and locations is based on our inner boundary condition of particle mirroring, which does not account for an ionospheric source. Inspecting some orbits in detail, we found orbits that included mirroring earthward of the inner box boundary. These orbits might actually have been of ionospheric origin. Furthermore, the peak of the beam population corresponds to particles with the lowest initial speeds and the limited resolution of this phase space region may not reveal enough particles with very small, initially tailward velocity.

In addition, the electric field in our simulation is solely the impulsive field associated with the dipolarization. Our simulation covers only a total period of tens of minutes and does not include a general convection electric field. The externally imposed electric field is used only to precondition the inner plasma sheet for the onset of reconnection; it is discontinued after $t = 61$ during the period studied for particle motion. Several studies have investigated the role of ionospheric sources in populating the plasma sheet. Using test particle motion in global MHD simulation fields (e.g., Huddleston et al., 2005; Moore et al., 2005; Péroomi-an et al., 2007) or multi-fluid MHD codes (e.g., Glocher et al., 2020; Welling & Ridley, 2010), it was found that global convection was effective in transporting ions of ionospheric origin through the lobes into the PSBL and the plasma sheet, typically at large distances.

The second location chosen for our investigation, which was closer to the plasma sheet boundary, has also been investigated earlier (Birn et al., 2015). It showed a single earthward field-aligned proton beam, together with an undisturbed core population, starting prior to the dipolarization. In contrast to the earlier results, we did not find a return beam, because in the present simulation, the delay from mirroring particles earthward of the inner box boundary was taken into account. This causes a delay of the return beam (Birn et al., 2019).

At this location closer to the boundary, oxygen ion beams were not as pronounced and delayed against the H^+ beam. The reason lies in the fact that the acceleration of these particles is found to be a direct, non-adiabatic, motion in the duskward electric field direction, which accelerates O^+ ions to the same energy as H^+ ions. Thus, O^+ ions get only 1/4 of the speed of the H^+ ions. After ejection along the field toward Earth they move more slowly and become more strongly displaced equatorward by the $\mathbf{E} \times \mathbf{B}$ drift. Also, depending on the characteristics of the RFT events, O^+ ions accelerated near the x-line may be slower than the propagating DF and thus, not be visible as a beam. It is noteworthy, however, that this acceleration mechanism would be more effective on multiply charged ions (Bingham et al., 2021).

In contrast to the hydrogen ions, the oxygen ion distributions did not exhibit visible return beams or even multiple beams at higher energy, which may result from multiple encounters with a DF (Birn et al., 2017). This is because the return beams and higher-energy beams require higher initial speed than the direct beam. Since we have assumed the same temperature for oxygen and hydrogen source populations, the initial oxygen thermal speed is lower by a factor of 1/4. Therefore, the initial and final oxygen phase space distributions fall off much more rapidly with velocity than the hydrogen distributions, and the potential return beams have f values too low to become observable.

In contrast to the particles close to the boundary, ions in the PSBL that encounter the propagating DF gain energy from this encounter comparable to the kinetic energy associated with the speed of the DF. If we assume maximum speeds of 500–1,000 km/s, this would yield a mass dependent acceleration of about 1–5 keV for protons and 20–80 keV for oxygen ions, independent of their charge state.

Data Availability Statement

Simulation results are available via <http://doi.org/10.5281/zenodo.4304668>.

Acknowledgments

The simulation work was performed at Los Alamos under the auspices of the US Department of Energy, supported by the NASA grants 80NSSC18K1452 and 80NSSC18K0834, and the NSF grant 1602655. DLT is thankful for support from NASA's MMS mission (contract NNG04EB99C). J. Birn is a Guest Scientist, Los Alamos National Laboratory.

References

- Andrews, M. K., Daly, P. W., & Keppler, E. (1981). Ion jetting at the plasma sheet boundary: Simultaneous observations of incident and reflected particles. *Geophysical Research Letters*, 8(9), 987–990. <https://doi.org/10.1029/GL008i009p00987>
- Bingham, S. T., Nikoukar, R., Cohen, I. J., Mauk, B. H., Turner, D. L., Mitchell, D. G., et al. (2021). Evidence for nonadiabatic oxygen energization in the near-Earth magnetotail from MMS. *Geophysical Research Letters*, 48. <https://doi.org/10.1029/2020GL091697>
- Birn, J., Chandler, M., Moore, T., & Runov, A. (2017). Ion velocity distributions in dipolarization events: Beams in the vicinity of the plasma sheet boundary. *Journal of Geophysical Research: Space Physics*, 122(8), 8026–8036. <https://doi.org/10.1002/2017JA024231>
- Birn, J., Chandler, M., & Nakamura, R. (2019). Ion beams in the plasma sheet boundary layer: MMS observations and test particle simulations. *Journal of Geophysical Research: Space Physics*, 125. <https://doi.org/10.1029/2019JA027113>
- Birn, J., Hesse, M., Bingham, S. T., Turner, D. L., & Nakamura, R. (2021). Acceleration of oxygen ions in dipolarization events: 1. CPS distributions. *Journal of Geophysical Research: Space Physics*, 126, e2021JA029184. <https://doi.org/10.1029/2021JA029184>
- Birn, J., Hesse, M., Runov, A., & Zhou, X. Z. (2015). Ion beams in the plasma sheet boundary layer. *Journal of Geophysical Research: Space Physics*, 120, 7522–7535. <https://doi.org/10.1002/2015JA021573>
- Birn, J., Nakamura, R., Panov, E. V., & Hesse, M. (2011). Bursty bulk flows and dipolarization in MHD simulations of magnetotail reconnection. *Journal of Geophysical Research*, 116, a–n. <https://doi.org/10.1029/2010JA016083>
- Forbes, T. G., Hones, E. W., Jr, Bame, S. J., Asbridge, J. R., Paschmann, G., Scokopke, N., & Russell, C. T. (1981). Evidence for the tailward retreat of a magnetic neutral line in the magnetotail during substorm recovery. *Geophysical Research Letters*, 8, 261–264. <https://doi.org/10.1029/gl008i003p00261>
- Frank, L. A., Ackerson, K. L., & Yeager, D. M. (1977). Observations of atomic oxygen (O^+) in the Earth's magnetotail. *Journal of Geophysical Research*, 82, 129–134. <https://doi.org/10.1029/ja082i001p00129>
- Glocer, A., Welling, D., Chappell, C. R., Toth, G., Fok, M. C., Komar, C., et al. (2020). A case study on the origin of near-Earth plasma. *Journal of Geophysical Research: Space Physics*, 125(11). <https://doi.org/10.1029/2020JA028205>
- Huddleston, M. M., Chappell, C. R., Delcourt, D. C., Moore, T. E., Giles, B. L., & Chandler, M. O. (2005). An examination of the process and magnitude of ionospheric plasma supply to the magnetosphere. *Journal of Geophysical Research*, 110(A12). <https://doi.org/10.1029/2004JA010401>
- Keika, K., Kasahara, S., Yokota, S., Hoshino, M., Seki, K., Nosé, M., et al. (2018). Ion energies dominating energy density in the inner magnetosphere: Spatial distributions and composition, observed by Arase/MEP-i. *Geophysical Research Letters*, 45(22), 12153–12162. <https://doi.org/10.1029/2018GL080047>
- Keika, K., Kistler, L. M., & Brandt, P. C. (2013). Energization of O^+ ions in the Earth's inner magnetosphere and the effects on ring current buildup: A review of previous observations and possible mechanisms. *Journal of Geophysical Research: Space Physics*, 118(7), 4441–4464. <https://doi.org/10.1002/jgra.50371>
- Kistler, L. M., Moukikis, C. G., Spence, H. E., Menz, A. M., Skoug, R. M., Funsten, H. O., et al. (2016). The source of O^+ in the storm time ring current. *Journal of Geophysical Research: Space Physics*, 121(6), 5333–5349. <https://doi.org/10.1002/2015JA022204>
- Kronberg, E. A., Grigorenko, E. E., Haaland, S. E., Daly, P. W., Delcourt, D. C., Luo, H., et al. (2015). Distribution of energetic oxygen and hydrogen in the near-Earth plasma sheet. *Journal of Geophysical Research: Space Physics*, 120(5), 3415–3431. <https://doi.org/10.1002/2014JA020882>

- Kronberg, E. A., Welling, D., Kistler, L. M., Mouikis, C., Daly, P. W., Grigorenko, E. E., et al. (2017). Contribution of energetic and heavy ions to the plasma pressure: The 27 September to 3 October 2002 storm. *Journal of Geophysical Research: Space Physics*, *122*(9), 9427–9439. <https://doi.org/10.1002/2017JA024215>
- Liao, J., Cai, X., Kistler, L. M., Clauer, C. R., Mouikis, C. G., Klecker, B., & Dandouras, I. (2014). The relationship between sawtooth events and O⁺ in the plasma sheet. *Journal of Geophysical Research: Space Physics*, *119*(3), 1572–1586. <https://doi.org/10.1002/2013JA019084>
- Liao, J., Kistler, L. M., Mouikis, C. G., Klecker, B., & Dandouras, I. (2015). Acceleration of O⁺ from the cusp to the plasma sheet. *Journal of Geophysical Research: Space Physics*, *120*(2), 1022–1034. <https://doi.org/10.1002/2014JA020341>
- Lyons, L. R., & Speiser, T. W. (2014). Evidence for current sheet acceleration in the geomagnetic tail. *Journal of Geophysical Research*, *87*, 2276–2286.
- Moore, T. E., Fok, M.-C., Chandler, M. O., Chappell, C. R., Christon, S. P., Delcourt, D. C., et al. (2005). An examination of the process and magnitude of ionospheric plasma supply to the magnetosphere. *Journal of Geophysical Research*, *110*. <https://doi.org/10.1029/2004JA010563>
- Nakamura, R., Baumjohann, W., Klecker, B., Bogdanova, Y., Balogh, A., Réme, H., et al. (2002). Motion of the dipolarization front during a flow burst event observed by Cluster. *Geophysical Research Letters*, *29*(4), 1942. <https://doi.org/10.1029/2002gl015763>
- Nosé, M., Lui, A. T. Y., Ohtani, S., Mauk, B. H., McEntire, R. W., Williams, D. J., et al. (2000). Acceleration of oxygen ions of ionospheric origin in the near-Earth magnetotail during substorms. *Journal of Geophysical Research*, *105*(A4), 7669–7677. <https://doi.org/10.1029/1999JA000318>
- Nosé, M., Ohtani, S., Lui, A. T. Y., Christon, S. P., McEntire, R. W., Williams, D. J., et al. (2000). Change of energetic ion composition in the plasma sheet during substorms. *Journal of Geophysical Research*, *105*(A10), 23277–23286. <https://doi.org/10.1029/2000JA000129>
- Orsini, S., Candidi, M., Formisano, V., Balsiger, H., Ghielmetti, A., & Ogilvie, K. W. (1984). The structure of the plasma sheet-lobe boundary in the Earth's magnetotail. *Journal of Geophysical Research*, *89*(A3), 1573–1582. <https://doi.org/10.1029/JA089iA03p01573>
- Peromian, V., El-Alaoui, M., Abdalla, M. A., & Zelenyi, L. M. (2007). A comparison of solar wind and ionospheric plasma contributions to the September 24–25, 1998 magnetic storm. *Journal of Atmospheric and Solar-Terrestrial Physics*, *69*(3), 212–222. (Global Aspects of Magnetosphere-Ionosphere Coupling). <https://doi.org/10.1016/j.jastp.2006.07.025>
- Peterson, W. K., Sharp, R. D., Shelley, E. G., Johnson, R. G., & Balsiger, H. (1981). Energetic ion composition of the plasma sheet. *Journal of Geophysical Research*, *86*, 761. <https://doi.org/10.1029/ja086ia02p00761>
- Quinn, J. M., & Southwood, D. J. (1982). Observations of parallel ion energization in the equatorial region. *Journal of Geophysical Research*, *87*, 10536–10540. <https://doi.org/10.1029/ja087ia12p10536>
- Reiff, P. H., Daou, A. G., Sazykin, S. Y., Nakamura, R., Hairston, M. R., Coffey, V., et al. (2016). Multispacecraft observations and modeling of the 22/23 June 2015 geomagnetic storm. *Geophysical Research Letters*, *43*(14), 7311–7318. <https://doi.org/10.1002/2016GL069154>
- Runov, A., Angelopoulos, V., Sitnov, M. I., Sergeev, V. A., Bonnell, J., McFadden, J. P., et al. (2009). THEMIS observations of an earthward-propagating dipolarization front. *Geophysical Research Letters*, *36*. <https://doi.org/10.1029/2009GL038980>
- Schödel, R., Baumjohann, W., Nakamura, R., Sergeev, V. A., & Mukai, T. (2001). Rapid flux transport in the central plasma sheet. *Journal of Geophysical Research*, *106*, 301–313. <https://doi.org/10.1029/2000JA900139>
- Takahashi, K., & Hones, E. W., Jr (1988). ISEE 1 and 2 observations of ion distributions at the plasma sheet-tail lobe boundary. *Journal of Geophysical Research*, *93*(A8), 8558–8582. <https://doi.org/10.1029/JA093iA08p08558>
- Welling, D. T., & Ridley, A. J. (2010). Exploring sources of magnetospheric plasma using multispecies MHD. *Journal of Geophysical Research*, *115*. <https://doi.org/10.1029/2009JA014596>
- Zhao, H., Li, X., Baker, D. N., Fennell, J. F., Blake, J. B., Larsen, B. A., et al. (2015). The evolution of ring current ion energy density and energy content during geomagnetic storms based on Van Allen Probes measurements. *Journal of Geophysical Research: Space Physics*, *120*(9), 7493–7511. <https://doi.org/10.1002/2015JA021533>
- Zhao, S. J., Fu, S. Y., Sun, W. J., Zhou, X. Z., Pu, Z. Y., Xie, L., et al. (2019). Oxygen ion butterfly distributions observed in a magnetotail dipolarizing flux bundle. *Journal of Geophysical Research: Space Physics*, *124*(10), 10219–10229. <https://doi.org/10.1029/2019JA027244>
- Zhou, X.-Z., Angelopoulos, V., Runov, A., Liu, J., & Ge, Y. S. (2012). Emergence of the active magnetotail plasma sheet boundary from transient, localized ion acceleration. *Journal of Geophysical Research*, *117*. <https://doi.org/10.1029/2012JA018171>